CERN Super Proton Synchrotron and an alternative design as prebooster ring for the future circular collider e^+e^- injector complex

O. Etisken*
CERN, 1211 Geneva, Switzerland and Kirikkale University, Kirikkale, Turkey

F. Antoniou, Y. Papaphilippou, T. Tydecks, and F. Zimmermann
CERN, 1211 Geneva, Switzerland

A. K. Ciftci
Izmir University of Economics, 35330, Izmir, Turkey

K. Oide
University of Geneva, 1211, Geneva, Switzerland

(Received 21 November 2022; accepted 6 July 2023; published 2 August 2023)

The Future Circular Collider (FCC) e^+e^- injector complex needs to produce and transport high-intensity e^+ and e^- beams at a fast repetition rate for topping up at collision energy. Two options are considered for a preaccelerator ring, to be used for an intermediate accumulation and acceleration before the bunches are transferred to the high-energy booster. One option is a slightly modified Super Proton Synchrotron (SPS), and the other is designing a new ring. We explore the needs and parameters of the existing SPS as prebooster ring and also develop a conceptual design of an alternative accelerator ring. After establishing the basic parameters, we describe the optics design and layout and discuss the single-particle linear and nonlinear dynamics optimization, including magnetic and alignment errors. In addition, we present synchrotron radiation power studies and analytical estimates of various collective effects for both prebooster ring design options, including space charge, intrabeam scattering, longitudinal microwave instability, transverse mode coupling instability, ion effects, electron cloud, and coherent synchrotron radiation.

DOI: 10.1103/PhysRevAccelBeams.26.081601

I. INTRODUCTION

A proposed high-luminosity high-energy circular electron-positron collider, Future Circular Collider (FCC) e^+e^- (FCC-ee), to be installed in a ~100 km tunnel, aims at extending the research currently being conducted at the present LHC [1]. The FCC-ee will deliver high luminosity to up to four experiments at center-of-mass energies ranging between 91.2 and 365 GeV and is conceived to serve as a general precision machine for the investigation of the Z, W, Higgs, and top particles [1–5]. The current injector complex design of the FCC-ee project consists of an e^+/e^- linac, which accelerates the beams up to 6 GeV, a prebooster ring (PBR), accelerating the beam from 6 GeV to about 16 GeV and a booster synchrotron ring (BR) integrated in the collider tunnel, accelerating the beams up to the collision energies. A schematic layout of the FCC-ee injector complex is shown in Fig. 1 [6].

Currently, the existing SPS is considered the baseline scenario for the prebooster ring of the injector complex, since it was the injector of the Large Electron-Positron Collider (LEP) [7] and it is still an operating machine [8,9] in the CERN accelerator complex. However, using the SPS as a prebooster ring imposes a series of challenges such as the possibly limited availability and scheduling conflicts (the SPS is presently used not only as LHC injector but also for several fixed-target experiments), synchrotron-radiation power issues due to the existing vacuum chamber and radiofrequency (rf) system requirements. To overcome these limitations, a new prebooster ring design has also been undertaken [10]: the "alternative" design. The optimum way forward will be decided in the following phases of the FCC project. In this document, we discuss the necessary modifications needed for the SPS, and we present the conceptual design of an alternative prebooster ring design. In addition, analytical estimates related to

*ozgur.etisken@cern.ch
Also at Izmir University of Economics, Izmir, Turkey.

Published by the American Physical Society under the terms of the Creative Commons Attribution 4.0 International license. Further distribution of this work must maintain attribution to the author(s) and the published article's title, journal citation, and DOI.

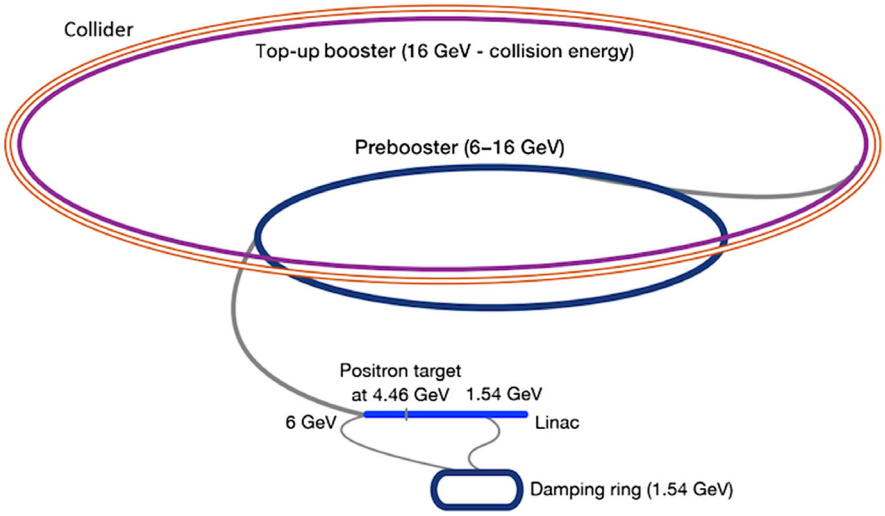

FIG. 1. A schematic layout of the FCC-ee injector complex [1].

collective effects, as well as SR power calculations, are made for both design options; the pertinent limitations are examined and highlighted.

II. DESIGN REQUIREMENTS

The purpose of the prebooster ring is to accommodate the 6-GeV beams coming from the linac and accelerate them up to 16 GeV before injection into the main booster ring. The design requirements of the PBR are, therefore, defined by the characteristics of the injected beam and the injection requirements of the upstream machine, the main booster ring.

The linac is designed to provide a 6-GeV beam with a transverse geometric emittance of 0.55 nm rad in the horizontal and 0.11 nm rad in the vertical plane. The rms energy spread (σ_δ) of the beam is 0.5% corresponding to an rms bunch length (σ_s) of 10 mm [6,11–13]. The beam properties at injection into the prebooster ring are summarized in Table I. Based on the energy spread of the injected beam and in order to minimize the injection losses in the PBR, a minimum energy acceptance of 1.5% (corresponding to $3\sigma_\delta$) is required. Moreover, the minimum dynamic aperture (DA) at PBR injection is imposed by the off-axis injection scheme to be 6.5 mm ($\beta_x = 8$ m) in the horizontal plane [14].

The cycle times including injection and extraction plateau, energy ramping of the SPS, and the alternative prebooster ring (see Sec. III) are around 0.8 s. The short injection plateau of around half a second imposes a short damping time at injection, of around 0.1 s [6,15]. The horizontal emittance and energy spread at the extraction energy of the PBR, on the other hand, are imposed by the dynamic aperture and energy acceptance at the injection of the main booster ring and limited to 5 nm rad and 0.3%, respectively [16]. Furthermore, the energy loss per turn is constrained not to exceed 30 MeV at the extraction energy to limit the rf power needed. In addition, the low magnetic field of the dipole magnets in the main booster ring, due to its large circumference (around 100 km, like the collider itself), is one of the important constraints that basically determine the extraction energy of the prebooster ring design. Figure 2 shows the minimum dipole field of the main booster ring as a function of the prebooster ring extraction energy. A dipole field of 50 G is considered a reasonable lower limit in terms of field stability. The 50-G

TABLE I. Linac beam parameters at injection into the PBR.

Parameters	Value
Energy (GeV)	6
Emittance (nm rad) (h/v)	0.55/0.11
Energy spread (%) (rms)	0.5
Bunch length (mm)	10

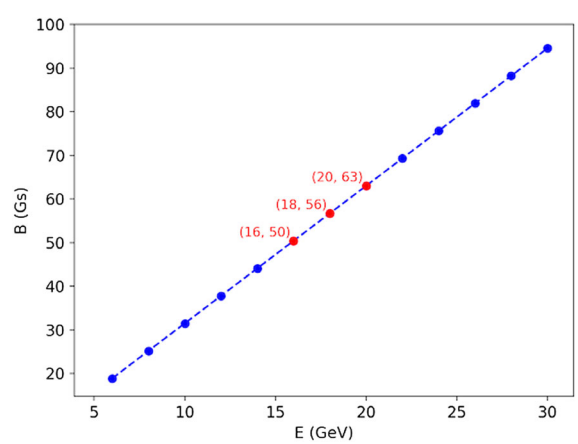

FIG. 2. Minimum magnetic field (B) of the main booster ring dipole as a function of the beam energy (E) at extraction from the prebooster ring.

TABLE II. FCC-ee PBR design requirements.

Required parameters	Value
Injection energy (GeV)	6
Extraction energy (GeV)	16
Damping time @ injection (hor.) (s)	0.1
Geo. emittance @ extraction (hor.) (nm rad)	5
Energy acceptance @ injection (%)	1.5
Dynamic aperture @ injection (hor.) (mm)	6.5
Energy spread @ extraction (%)	0.3

field corresponds to a PBR extraction energy of 16 GeV. Extraction energies of 18 and 20 GeV were also studied and these are discussed in Sec. IV E. Table II summarizes the design requirements for the FCC-ee PBR.

III. INJECTION FILLING SCHEMES THROUGHOUT THE INJECTOR COMPLEX

The FCC-ee collider should deliver high luminosity for up to four experiments at four different beam energies, that is, at the Z pole (45.6 GeV), the WW threshold (80 GeV), when operated as a Higgs factory (120 GeV), and at the $t\bar{t}$ threshold (182.5 GeV) [1]. Table III summarizes the injection scheme parameters of the injector complex for the different collider beam energies and filling modes. The parameters are calculated considering either the SPS (SPS-PBR) or the alternative design (A-PBR), separately, as the prebooster ring. A linac bunch population of 2.13×10^{10} particles is required for both e^+ and e^-, and the linac accelerates 1 or 2 bunches with a 100- or 200-Hz repetition rate. After acceleration in the linac, the beams are transferred between 40 and 328 times into the A-PBR, or between 48 and 595 times into the SPS-PBR, in order to fully fill the respective PBR with the required number of bunches.

The required number of bunches and, therefore, the injection time into the PBR depend on the mode (Z, W, H, $t\bar{t}$). The total number of bunches varies from 48 to 320 for the A-PBR, and from 48 to 1190 for the SPS-PBR, respectively. These numbers correspond to 1–52 main-booster injections from the A-PBR, and 1–14 injections from the SPS-PBR, to fill the required 48–16,640 bunches in the main booster ring. The most challenging case in terms of bunch intensity and number of bunches is the Z mode of operation. Both PBR options feature a 400-MHz rf system. The ramping time of 0.125 s is based on the SPS experience during the years of the Large Electron-Positron Collider (LEP). The minimum bunch spacing is defined as 15, 17.5, or 20 ns.

The overall duty factor for the SPS-PBR varies between 5% for the $t\bar{t}$ mode and 76% for the Z mode, which is a compelling parameter for the SPS ring. On the other hand, the injector layout with the A-PBR would not impact the SPS' current and/or any other planned future operation. The cycle times for both options are short, especially for the $t\bar{t}$ mode. This cycle length imposes a short damping time which should be around 0.1 s. This is a challenging value for the SPS ring as discussed in Sec. IV. The injection process through the various accelerators of the FCC-ee

TABLE III. The FCC-ee injection scheme parameters.

Parameters (unit)	Z	W	H	tt
Beam energy (GeV)	45.6	80	120	182.5
Filling type	Initial/Top-up	Initial/Top-up	Initial/Top-up	Initial/Top-up
Bunch population ($\times 10^{10}$)	2.13/1.06	0.94/0.56	0.94/0.56	1.38/0.82
Linac bunches/pulse	2	2	1	1
Linac repetition rate (Hz)	200	100	100	100
Number of linac injection with the SPS-PBR	594/595	500	328	48
SPS-PBR minimum bunch spacing (ns)	15/17.5/20	22.5	67.5	450
Number of SPS-PBR cycles	14	2	1	1
Number of SPS-PBR bunches	1188/1190	1000	328	48
SPS-PBR cycle time (s)	3.3	5.4	3.6	0.8
SPS-PBR duty factor	0.76	0.49	0.23	0.05
Filling time (inlc. the SPS-PBR) (s)	958/95.9	520/26	277.2/13.9	227.7/11.4
Number of linac injection with A-PBR	160	50	164	48
A-PBR minimum bunch spacing (ns)	20	65	40	137.5
Number of A-PBR cycles	52	20	2	1
Number of A-PBR bunches	320	100	164	48
A-PBR cycle time (s)	1.15	0.85	1.99	0.83
A-PBR duty factor	0.98	0.77	0.26	0.05
Filling time (incl. the A-PBR) (s)	1224/122	722/38	291/14	227/11
Number of BR/collider bunches	16640	2000	328	48
Number of BR cycles	10/1	20/1	20/1	20/1

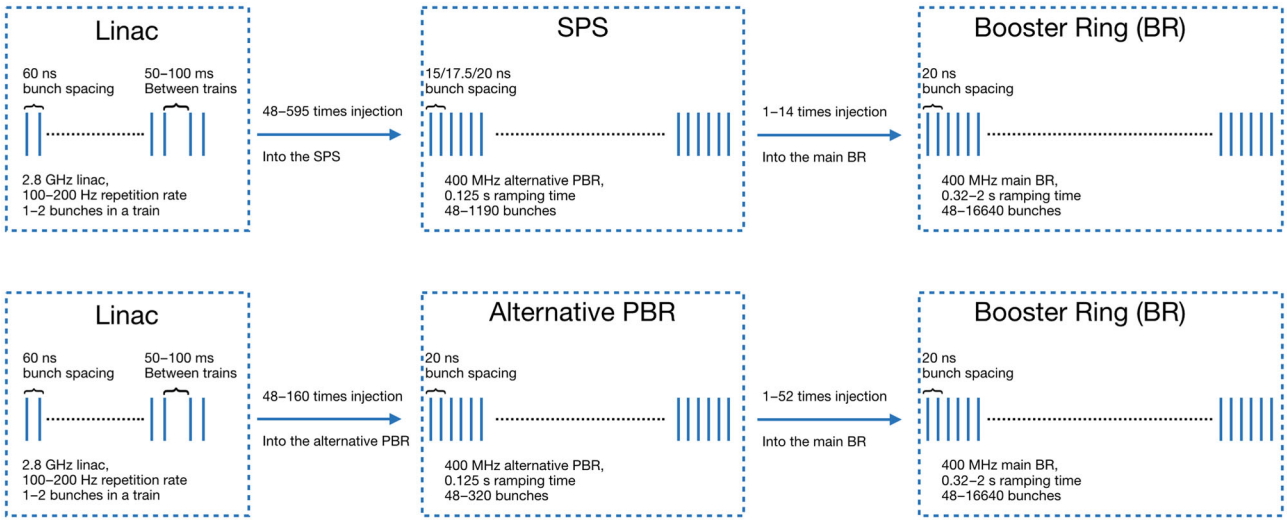

FIG. 3. The FCC-ee injector scheme with either the SPS-PBR (top) and the A-PBR (bottom).

injector complex is schematically shown in Fig. 3, with either the SPS-PBR (top) or the A-PBR (bottom).

IV. THE SPS AS PREBOOSTER RING (SPS-PBR)

The Super Proton Synchrotron (SPS) is the second largest accelerator in the current CERN accelerator complex. The SPS was initially used as a proton synchrotron, then as a proton-antiproton collider, and later also as the injector for the Large Electron-Positron Collider (LEP) [7,17]. At present, it provides beams to the Large Hadron Collider (LHC) and to several fixed target experiments [8,9]. It was, therefore, naturally considered the baseline option for the PBR of the FCC-ee injector complex [15]. In this section, we investigate the possibility of using the existing SPS as a PBR (SPS-PBR), address possible challenges, and propose a few necessary modifications to overcome the expected challenges.

A. Optics design

The SPS synchrotron has a circumference of 6911.5 m. It consists of six sextants, each one composed of 18 FODO cells and 2 dipole-free cells. Dispersion suppression is achieved in the straight sections by keeping the total arc phase advance a multiple of 2π [18,19]. Applying an energy scaling to the existing SPS design and taking into account the design requirements of the PBR (see Table II), two main challenges were revealed: the horizontal geometric emittance at extraction is 74 nm rad, which is 15 times larger than the required one and the synchrotron radiation damping time at injection is 1.8 s, 18 times longer than the one required for the PBR. In this respect, a phase advance optimization and the installation of damping Wiggler (DW) and Robinson wiggler (RW) magnets were proposed [10], which will be discussed next.

1. Phase advance optimization

The circumference and, therefore, the bending radius (ρ) of the machine is fixed for the SPS. The optimization of the emittance can thus be achieved by minimizing the fifth radiation integral (I_5) by optimizing the phase advance of the arc cells. The minimum horizontal emittance is achieved for a horizontal phase advance of around $\mu_x = 0.37/2\pi$ [20–22], while the current operational phase advance of the SPS FODO cell is around $\mu_x = 0.25/2\pi$. By this change of phase advance, the geometrical emittance at the extraction energy can be reduced from 75 to 34 nm rad, while satisfying at the same time the condition for the dispersion suppression. This reduction is, however, not enough, as the required geometrical emittance at extraction is 5 nm rad.

2. Damping and Robinson wiggler magnets

The horizontal emittance can be further decreased by introducing damping wiggler magnets at locations with zero (or very small) dispersion, which contribute to the synchrotron radiation integrals as [23,24]:

$$I_{2w} = \frac{1}{(B\rho)^2}\frac{B_w^2 L_w}{2}, \qquad I_{3w} = \frac{4L_w}{3\pi\rho_w^3},$$
$$I_{4w} = -\frac{3}{32\pi^2}\frac{\lambda_w^2}{\rho_w^4}Lw \quad \text{and} \quad I_{5w} = \frac{\lambda_w^2}{15\pi\rho_w^5}\langle\beta_x\rangle L_w. \qquad (1)$$

Here, B_w denotes the peak magnetic field, L_w the total damping wiggler length, ρ the bending radius, and B the magnetic field of the main dipole magnets, $\langle\beta_x\rangle$ the average beta function at the damping wiggler section, $\rho_w = B\rho/B_w$, and λ_w the damping wiggler period.

Figure 4 shows an analytical parameterization of the horizontal emittance (top-left), the energy loss per turn

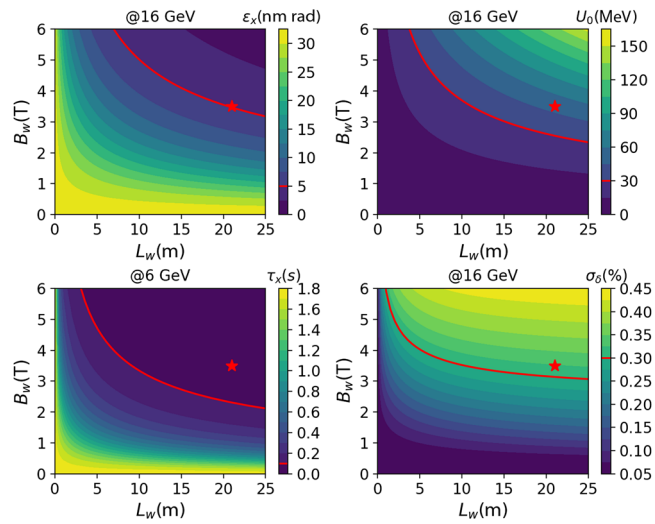

FIG. 4. Analytical parametrization of the horizontal emittance (top-left), energy loss per turn (top-right), and energy spread (bottom-right) at extraction energy as well as the horizontal damping time (bottom-left) at injection energy, as a function of the total wiggler length (L_w) and the wiggler peak field (B_w). The red contours indicate the required values of each parameter. The red stars illustrate essential damping wiggler magnet characteristics to reach the required parameters.

(top-right), and the energy spread (bottom-right) at extraction energy as well as the horizontal damping time (bottom-left) at injection energy, with the total wiggler length and peak field. The required output emittance of 5 nm rad can be achieved for a total wiggler length of 21 m and a wiggler peak field of 3.5 T. For this set of parameters, a very short damping time is also achieved ($\tau_x < 0.1$ s). The energy loss per turn, on the other hand, is very much enhanced ($U_0 \approx 50$ MeV), which would require a demanding rf system to compensate for these losses. At the same time, the energy spread is also increased.

Another way to modify the synchrotron radiation integrals is by introducing Robinson wiggler (RW) magnets, as proposed in [25,26]. The RWs are composed of a series of combined function magnets. They act on the damping partition ($D = I_4/I_2$), by modifying the fourth synchrotron radiation integral (I_4). If including RW magnets, the damping partition can be expressed as [27,28]:

$$D = \frac{\rho\langle D_x\rangle}{\pi(B\rho)^2}\int_0^{L_w} B_z \frac{dB_z}{dx}\, ds. \tag{2}$$

Based on Eq. (2), if a RW is placed at a location with nonzero dispersion, the damping partition is modified and the horizontal emittance can be further decreased, however, at the cost of an increased energy spread [25,27–31]. This puts a limit on the maximum number of Robinson wiggler magnets that can be used in the ring. Taking this into account, a combination of DW and RW magnets was proposed for achieving the required horizontal

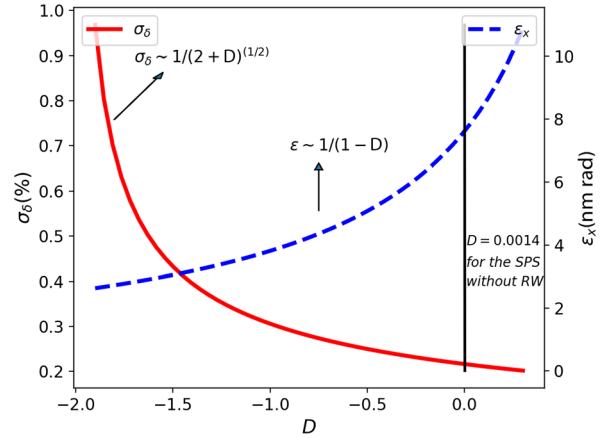

FIG. 5. Horizontal emittance and energy spread at extraction as a function of the damping partition number D for the effect of RW as well as already 3.5 T, 12.15-m damping wiggler.

emittance at extraction and the damping time at injection energy, while keeping the energy loss per turn within requirements [10].

Figure 5 shows an analytical parameterization of the horizontal emittance (blue) and energy spread (red) with the damping partition D, including damping and Robinson wiggler magnets. The damping partition without RW is 0.0014 and is indicated by the solid black line. By adding RW wiggler magnets D becomes negative, depending on the RW characteristics. The required horizontal emittance at extraction is obtained for $D = -1$. This can be achieved for a peak field of 0.5 T, a total length of 6 m, and a gradient of 75 T/m.

The damping wiggler magnets are installed at locations with minimum dispersion, as shown in Fig. 6. Their peak

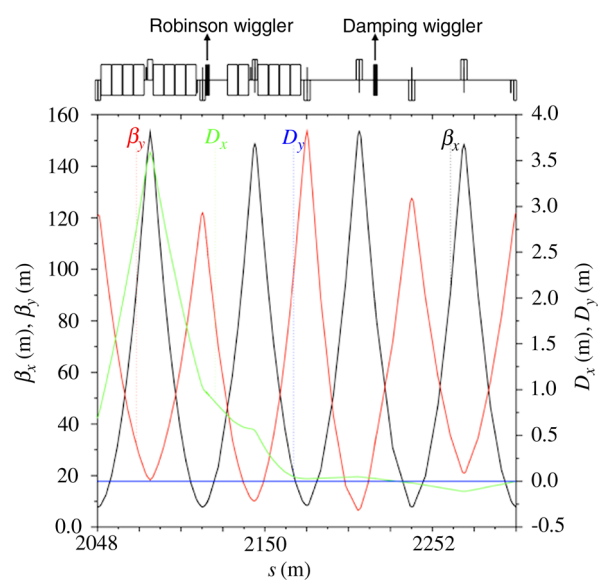

FIG. 6. Optics functions of the last four cells of one sextant of the SPS, indicating the locations of the DW and RW magnets.

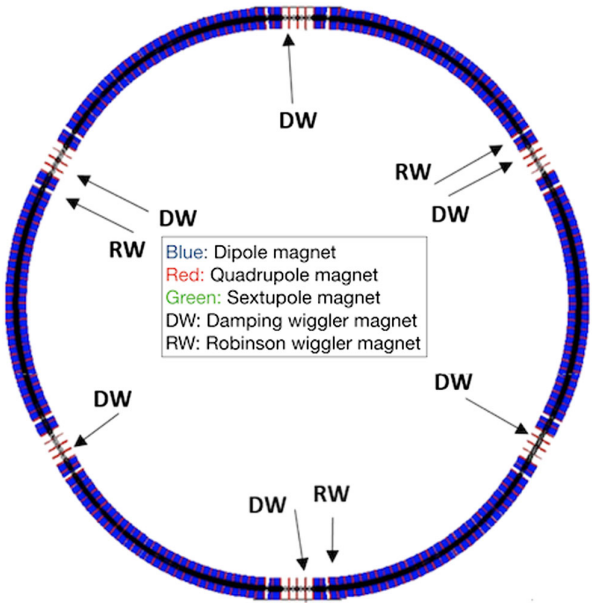

FIG. 7. The layout of the SPS-PBR indicating the locations of the DW and RW magnets.

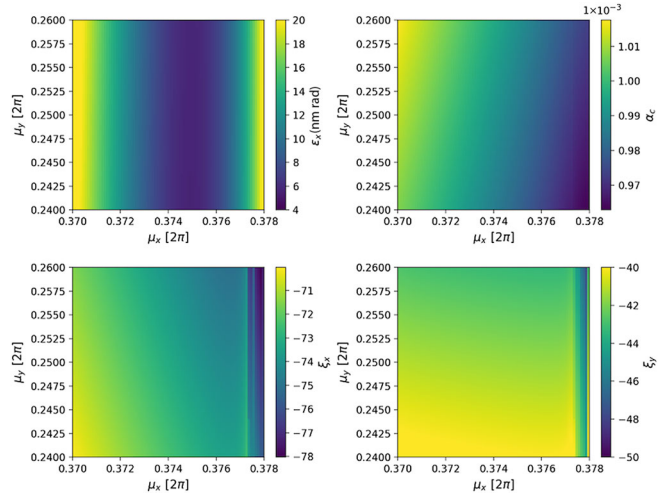

FIG. 8. Horizontal emittance (top-left), momentum compaction factor (top-right), natural horizontal (bottom-left), and vertical (bottom-right) chromaticities as a function of the horizontal and vertical phase advances for the SPS FODO cell.

field was chosen at 3.5 T for a total wiggler length of 12.15 m. By this combination of DW and RW magnets, the required horizontal emittance and damping time are achieved and the energy loss per turn and equilibrium energy spread at extraction are kept within the requirements. Three RW magnets and six DW magnets are installed in the straight sections of the ring, as shown in Fig. 7. Corrector magnets have also been foreseen for local correction of the linear optics distortion introduced by the wiggler magnets. Thus, the required parameters are met by inserting viable DWs and RWs into the existing SPS design.

A fine scan of the phase advance was performed, including DW and RW magnets, to define the optimal working point and the area for the required horizontal emittance. The scan was performed around $\mu_x = 0.375/2\pi$ (achromatic condition) and $\mu_y = 0.25/2\pi$. Figure 8 shows the dependence of the horizontal emittance (top-left), the energy loss per turn (top-right), and the horizontal (bottom-left) and vertical (bottom-right) chromaticities on the horizontal and vertical phase advances. Only a limited phase advance area around $\mu_x = 0.375/2\pi$ can provide the required emittance at extraction. An optimal phase advance of $(\mu_x, \mu_y) = (0.3747/2\pi, 0.24/2\pi)$ was finally chosen. As the achromatic condition is not strictly achieved by this choice, a small dispersion leakage is introduced, as shown in Fig. 6. Within the range of the phase advance scan, the impact on the natural chromaticity is small in both planes.

B. Dynamic aperture

The dynamic aperture (DA) of the ring is mainly defined by the sextupoles that are used for the chromatic correction [20]. A pair of sextupoles is installed at locations with large dispersion in each of the arc FODO cells. The working point in the tune diagram corresponding to the chosen phase advance is $(Q_x, Q_y) = (40.38/26.71)$. Figure 9 (top) shows the tune working point (black) on a resonance diagram up to third order, defined by the resonance condition [20]:

$$(j-k) \times Q_x{}^{\mathrm{cell}} + (l-m) \times Q_y{}^{\mathrm{cell}} = P \times n, \qquad (3)$$

where j, k, l, m, n are integer numbers and P is the superperiodicity of the lattice. Systematic resonances are shown in red, while nonsystematic ones in blue. Solid lines correspond to normal resonances while dashed lines correspond to the skew ones. The chromatic tune shift for off-momentum particles with $\Delta p/p$ up to $\pm 1.5\%$ is indicated by the green dots.

Due to the number of bunches needed to be stored in the PBR, an off-axis (on-energy) injection method was proposed, imposing a minimum DA of 6.5 mm [32,33]. MAD-X/PTC tracking simulations were performed, including the chromaticity sextupoles and fringe fields. Particles with different initial conditions were tracked for 4400 turns (around 1 damping time), for $\Delta p/p = 0$, 1.5%, and −1.5%, and the results are shown in Fig. 9. An adequate DA of 10 mm in the horizontal ($\beta_x = 8$ m) and 20 mm in the vertical plane ($\beta_y = 120$ m) can be achieved.

C. Transverse acceptance

The minimum transverse acceptance required for Gaussian bunches can be calculated by [24,34–36]:

$$R_{\mathrm{acc}} = 5\sqrt{\beta_{x,y}\epsilon_{\mathrm{rms}}} + 3D_{x,y}(\delta p/p_0)_{\mathrm{rms}}, \qquad (4)$$

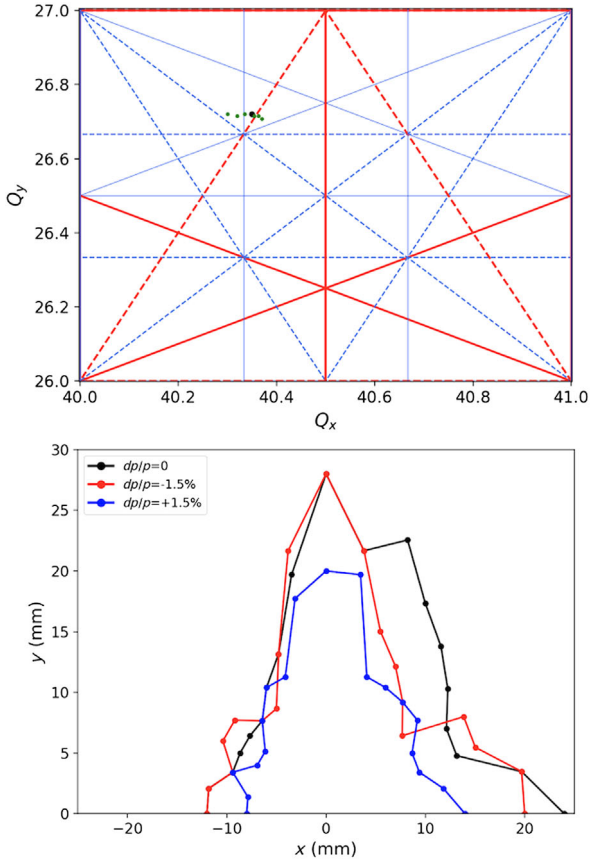

FIG. 9. Tune working point on a resonance diagram up to third order and dynamic aperture. Systematic (red), nonsystematic (blue), normal (solid), and skew (dashed) resonances are shown. The black point shows the working point, while the green points indicate the tune shift with off momentum up to $\pm 1.5\%$ (top). The on-momentum and off-momentum dynamic aperture of the SPS for $\delta \equiv \Delta p/p = 0$ (black), 1.5% (blue), and -1.5% (red) (bottom).

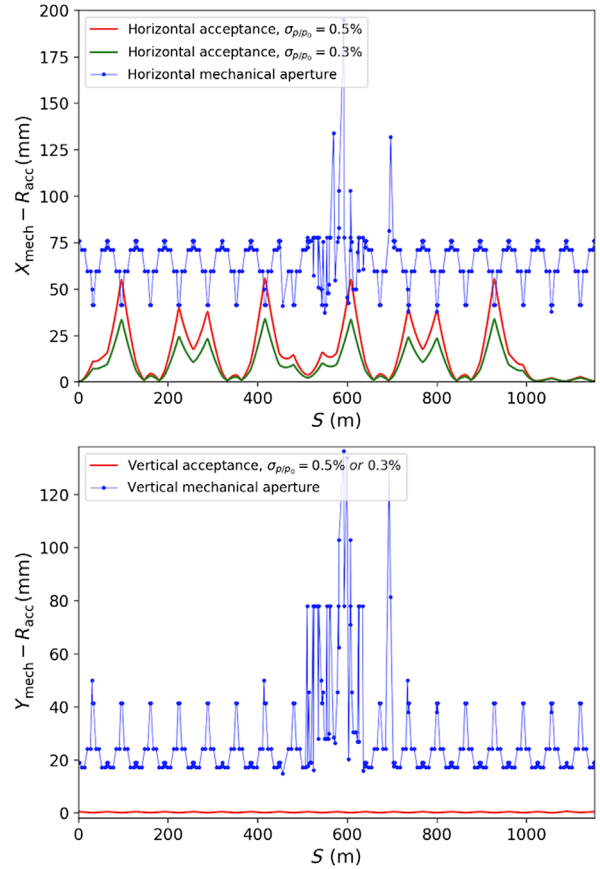

FIG. 10. Horizontal (top) and vertical (bottom) acceptance (R_{acc}) of the SPS-PBR together with the existing horizontal (top) and vertical (bottom) vacuum chamber X_{mech}/Y_{mech}).

where ϵ_{rms} is the rms emittance, $\Delta p/p_0$ the rms energy spread of the incoming beam, $D_{x,y}$ the dispersion function, and $\beta_{x,y}$ the betatron functions in the horizontal (x) and vertical (y) planes, respectively.

Based on the SPS optics design, the horizontal (top) and vertical (bottom) acceptance around one sextant of the SPS ring are shown in Fig. 10. The existing mechanical aperture of the SPS is also shown in blue. For an energy spread of $\delta p/p_0 = 0.5\%$ (red), which is the one achieved by the current linac design, the mechanical aperture is smaller than the transverse acceptance, at the locations of the quadrupoles [37]. In order to ensure that the transverse acceptance required remains smaller than the mechanical aperture of the ring, an energy spread of no more than 0.3% is needed. This requirement must be taken into account for the linac design. In fact, due to the large horizontal dispersion in the arcs, the transverse acceptance is dominated by the energy spread, while the sensitivity to the incoming transverse emittance is much smaller. In the vertical plane, where the design vertical dispersion is zero, the required acceptance is always smaller than the mechanical aperture of the machine.

D. rf voltage and energy acceptance

The longitudinal momentum acceptance of the ring is defined by [38]

$$\left(\frac{\delta_E}{E}\right)^2 = \pm\left[\frac{qV((2\cos\phi_s) + (2\phi_s - \pi)\sin\phi_s)}{\pi h \alpha_c E_0}\right], \quad (5)$$

where V signifies the rf voltage, h the harmonic number, α_c the momentum compaction factor, E the beam energy, and ϕ_s the rf phase:

$$\phi_s = \arcsin\left(\frac{U_0}{V_0}\right). \quad (6)$$

To get an adequate momentum acceptance and consequently, an optimal injection efficiency, a large rf voltage or a small momentum compaction factor is needed. Figure 8 (top-right) shows the momentum compaction factor as a function of the phase advance. Figure 11 presents the

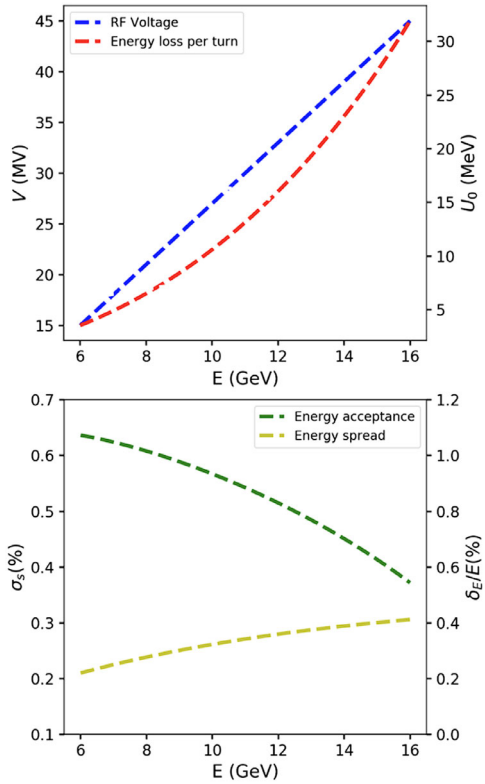

FIG. 11. The energy loss per turn (U_0) and rf voltage (V_{rf}) (top), energy spread (σ_s), and energy acceptance ($\Delta E/E$) (bottom) for the energy cycle.

dependence of the rf voltage and energy loss per turn (top) together with energy spread and energy acceptance (bottom) on the beam energy, along the SPS energy cycle. The energy loss per turn ranges from 3.4 to 31.5 MeV. To achieve an energy acceptance of 1%, the minimum rf voltage is set to 15 MV at injection and it increases linearly up to 45 MV at extraction energy. Through this choice, the equilibrium rms energy spread is always lower than the energy acceptance during the energy ramping, as shown by the bottom plot of Fig. 11. This figure indicates that at extraction, the energy acceptance is about twice the rms energy spread, which may imply an unacceptably low quantum lifetime. For a decent quantum lifetime, the energy acceptance should be at least 6 times the rms energy spread [38]. This would imply a need to increase the rf voltage to about 145 MV. This should be investigated in the future.

E. Different extraction energy options

Different options for the PBR extraction energy were also investigated and the impact on the main design parameters is summarized in Table IV. One of the determinant parameters for the choice of extraction energy for the PBR is the magnetic field at injection into the main booster ring. As shown in Fig. 2, $B = 50$ Gauss would be the booster dipole field needed at 16 GeV and 63 Gauss the field at 20 GeV [16,39]. The liability of such low magnetic fields of the main booster dipoles should be investigated through prototyping in the following phases of the project. For the 20 and 18-GeV options, the energy loss per turn is very high, implying an even more demanding rf system. The equilibrium energy spread at extraction also exceeds the energy acceptance of the main booster ring, for both 18 and 20 GeV.

Based on the above considerations, the 16-GeV option was finally chosen as the baseline, as it provides reasonable energy spread, energy loss per turn, and emittance at extraction. Table V summarizes the main performance parameters of the SPS as an FCC-ee prebooster ring, for the 16-GeV option, with a still marginal rf voltage, which might need to be substantially increased for obtaining a decent beam lifetime. The SPS has been used to feed several fixed-target experiments, as a collider ring, and/or a part of injector complex since 1979, when the SPS went into operation. It has worked successfully, including its contributions to the Nobel-prize-winning discovery of W and Z particles at CERN. As a core element in the current CERN accelerator complex, the SPS provides beams for several experiments as well as the Large Hadron Collider (LHC). Regardless, the SPS as an existing and long-standing machine may offer cost advantages, while it comes with several challenges, as explained. Thus, another new, smaller prebooster ring has been designed as an alternative option (A-PBR).

TABLE IV. Comparison of the SPS-PBR beam parameters for different extraction energies.

Parameters	20 GeV	18 GeV	16 GeV
Horizontal geo. emittance (nm rad) @ extraction energy	5.92	5.60	5.64
Energy loss per turn (MeV) @ extraction energy	128.0	73.9	31.5
Horizontal damping time (s) @ injection energy	0.003	0.005	0.01
Equilibrium energy spread (%) @ extraction energy	0.6	0.5	0.38
rf voltage (MV) @ extraction energy	160	90	45
Damping wiggler field (T)	6	5	3.5
Damping wiggler length (total) (m)	12.15	12.15	12.15
Robinson wiggler field (T)	0.5	0.5	0.5
Robinson wiggler length (total) (m)	12	12	6

TABLE V. The performance parameters of the SPS-PBR.

Parameters	Injection		Extraction
Beam energy [E (GeV)]	6		16
Circumference [C (m)]		6911.5	
Horizontal geo. emittance [ϵ_x (nm rad)]	0.73		5.6
Damping times ($h/v/l$) [$\tau_{h/v/l}$ (s)]	0.03/0.03/0.015		0.01/0.01/0.005
Momentum spread (σ_δ)	0.3×10^{-2}		0.38×10^{-2}
Energy loss per turn [U_0 (MeV)]	3.4		31.5
Natural chromaticities (h/v) ($\xi_{h/v}$)	$-72/-40$		$-72/-40$
Bunch length [σ_z (m)]	0.041		0.055
Tunes ($h/v/s$) ($Q_{h/v/s}$)		40.38/26.71/0.08	
Dynamic aperture (h/v) [DA (mm)]	10/20		...
rf frequency [F_{rf} (MHz)]		400	
rf voltage [V_{rf} (MV)]	15		45
Harmonic number (h)	9215		9215
Momentum compaction factor (α_c)	0.98×10^{-3}		0.98×10^{-3}
Energy acceptance [$\frac{\delta E}{E}$ (%)]	1.0		0.55
Bending magnet length [l_{bend} (m)]		6.26	
Field of bending [B_{dipole} (T)]	0.026		0.071
Number of bending magnets (N_{bend})		744	
Damping wiggler length (total) [L_{dw} (m)]		12.15	
Damping wiggler field [B_{dw} (T)]		3.5	
Number of damping wiggler magnets (N_{dw})		6	
Damping wiggler period [λ_{dw} (m)]		0.05	
Robinson wiggler length (total) [L_{rw} (m)]		6	
Robinson wiggler field [B_{rw} (T)]		0.5	
Number of Robinson wiggler magnets (N_{rw})		3	

V. THE ALTERNATIVE PREBOOSTER RING DESIGN (A-PBR)

In parallel to the SPS design option, a "green field" alternative prebooster ring (A-PBR) design was also studied, which can overcome some of the main limitations of the SPS-PBR, such as the machine scheduling and availability conflicts, the strong synchrotron radiation power, which cannot be sustained with the existing vacuum chamber of the SPS (as discussed in Sec. VI), and a demanding rf system upgrade, with a voltage possibly exceeding 145 MV. In this section, the conceptual design of the A-PBR is described.

A. Parameter scaling

Based on the injection and extraction requirements specified in Table II, the scaling of main parameters such as horizontal emittance (ϵ_x), energy loss per turn (U_0), equilibrium energy spread (σ_δ) at extraction, and horizontal synchrotron radiation damping time (τ_x) at injection, as a function of the machine circumference (C), and the ring filling factor (F) can be established. This is an important step to further determine the layout of the ring and to deduce the key parameters of the main lattice cell. To this end, Fig. 12 shows the parametrization of the horizontal emittance at extraction energy with the ring circumference and the filling factor. As expected, the higher filling factor

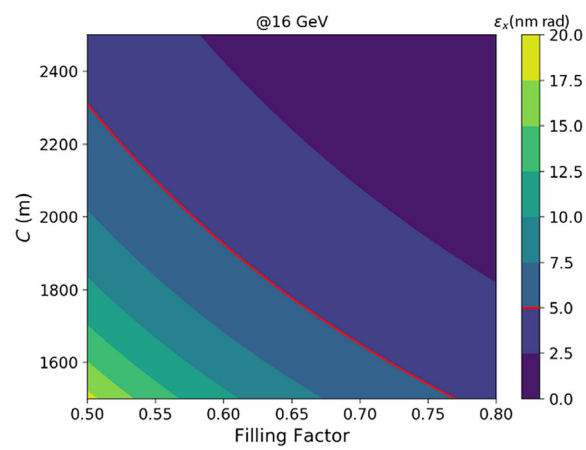

FIG. 12. Analytical parameterization of the horizontal emittance at extraction energy with filling factor (F) and circumference (C). The red contours correspond to the required value.

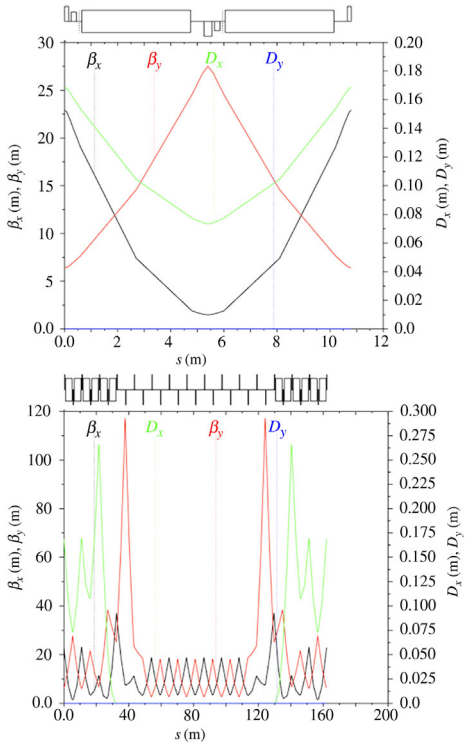

FIG. 13. The optical functions of the main FODO cell in the arc (top) and straight section (bottom) for the A-PBR.

allows a lower emittance for a shorter ring circumference. For a typical filling factor of around 0.6, the corresponding circumference is around 2.0 km. This choice is optimal, as it provides the minimum circumference for a limited rf power while satisfying the transverse emittance, damping time, and energy spread requirements.

B. Optics design and layout

The ring layout consists of four identical arcs and straight sections. Therefore, it has a superperiodicity of 4. Each of the four arcs features 32 FODO cells with a length of 10.8 m, consisting of two 4.1 m-long dipoles sandwiched between quadrupoles with 30 cm length. The ring has a total circumference of 2030.4 m. The dipole field at injection energy is 0.10 T increasing up to 0.27 T at extraction energy. Two families of 20-cm long sextupoles are installed in the dispersive regions for compensation of the natural chromaticity. Each straight section consists of five cells and reserves sufficient space to accommodate the rf, injection, and extraction elements. Figure 13 shows the optical function of straight section (bottom) and one FODO in the arc (top). Optics and dispersion matching are achieved through special adjustable optics cells at the interface between the arcs and the straight sections. The optical functions of the one superperiod are shown in Fig. 14. The layout of the A-PBR, with a superperiodicity of 4, is shown in Fig. 15.

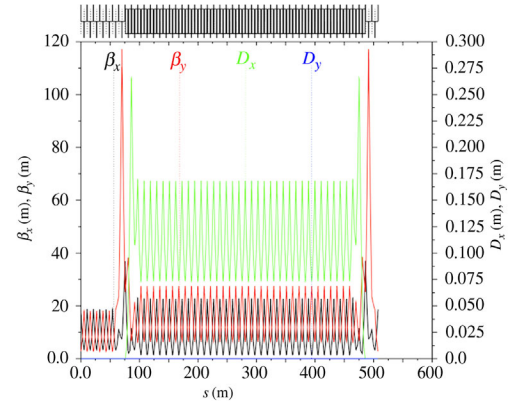

FIG. 14. The optical functions of the one-superperiod lattice of the A-PBR.

C. Phase advance optimization

The equilibrium horizontal emittance of the ring is mainly determined by the cells in the arcs. Similar to the case of the SPS, a phase advance scan was performed. The impact on the equilibrium horizontal emittance is illustrated in Fig. 16. Figure 17 shows the dependence of the horizontal (top-left) and vertical (top-right) chromaticities ($\xi_{x/y}$), the momentum compaction factor (α_c) (bottom-left), and the quadratic sum of tune shift with amplitude (bottom-right) on the horizontal and vertical phase advances of the arc FODO cell. This important step makes sure that we choose optimal values for the tune working point and for other parameters, such as emittance, momentum compaction factor, etc. In this case, the natural chromaticities are a factor of 2 higher than for the SPS case. The amplitude dependent tune shift was calculated using the anharmonicity values from MAD-X/PTC [40].

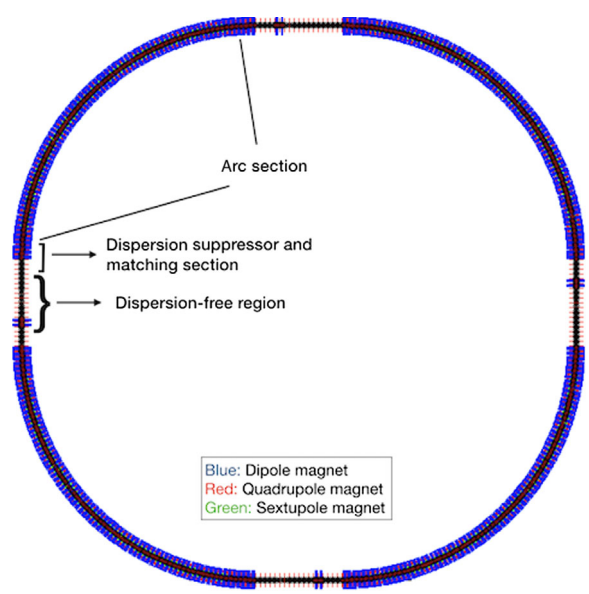

FIG. 15. The layout of the A-PBR.

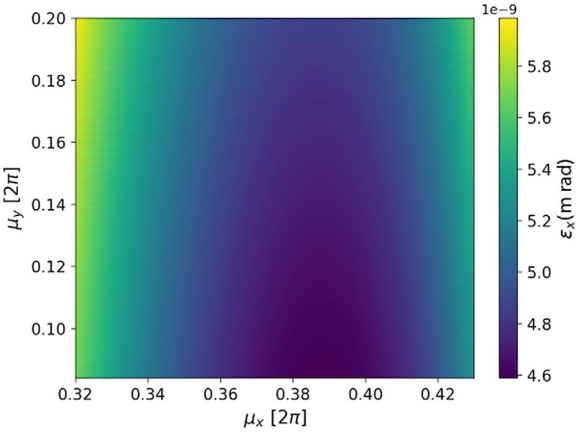

FIG. 16. Horizontal emittance as a function of the horizontal and vertical phase advances in the arc for the A-PBR.

The optimal horizontal phase advance in the arc is chosen around $\mu_x = 0.383/2\pi$ (135^0) per cell for achieving a small emittance at extraction, while keeping the chromaticities and the detuning with amplitude as low as possible. The phase advance in the straight section is set close to $\mu_x = 0.25/2\pi$ (90^0) per cell to minimize the betatron functions and to maximize the efficiency of the injection and extraction elements.

D. Dynamic aperture

1. Bare lattice

Two families of sextupole magnets for chromaticity correction are located in dispersive regions of the arcs of the A-PBR. Unlike for the SPS case, the dispersion in the A-PBR is small. This, in combination with the higher chromaticity, leads to much stronger sextupole strengths, and thus stronger nonlinear effects.

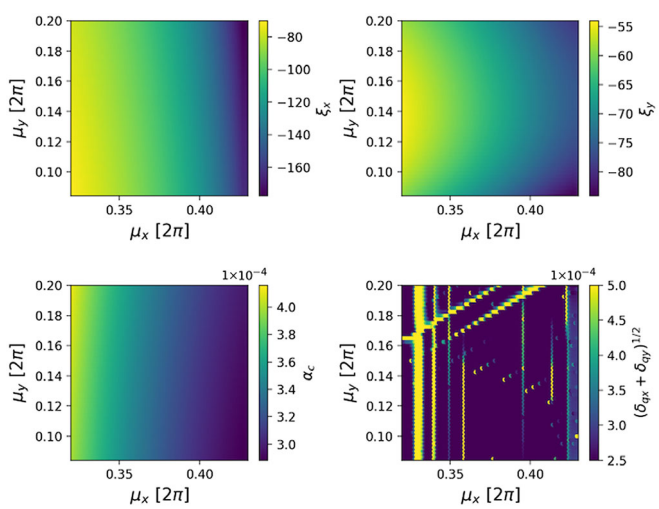

FIG. 17. Parametrization of chromaticity (top), momentum compaction factor (bottom-left), tune shift with amplitude (bottom-right) as a function of the horizontal and vertical phase advances for the A-PBR arc.

The working point (WP) optimization is performed by tuning the phase advance of the FODO cell in the straight sections. Figure 18 (top) shows the resonance diagram for horizontal tunes ranging from 24 to 28, and vertical tunes between 60 and 64, taking into account the superperiodicity ($P = 4$) of the lattice. Based on the density of the systematic resonance lines, integer tunes of $(Q_x, Q_y) = (63, 27)$ were chosen. Figure 18 (bottom) shows the final tune working point (black dot). In the resonance diagrams, the systematic resonances are shown in red and the nonsystematic in blue. Solid lines represent the normal while dashed lines the skew resonances. The green points show the tune of off-momentum particles with $\Delta p/p$ of up to $\pm 1.5\%$.

Dynamic aperture simulations were conducted for the bare lattice, including the chromaticity sextupoles and

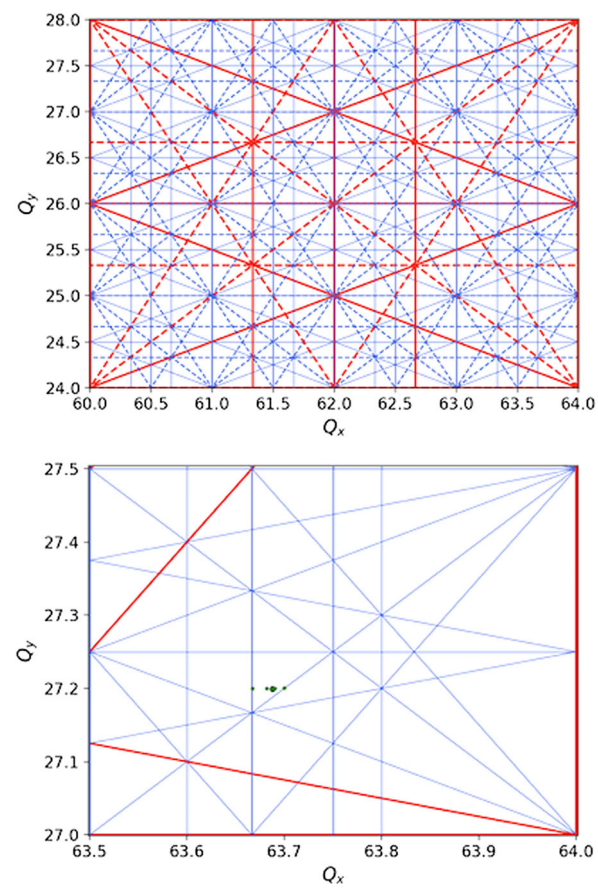

FIG. 18. Resonance diagrams up to third order for different integer tunes ($Q_x, Q_y = 60/64, 24/28$) for periodicity of four for the A-PBR design. Systematic (red), nonsystematic (blue), normal (solid), and skew (dashed) resonances are shown (top). Tune working point (WP) on a resonance diagram up to the fifth order. The black point shows the WP and the green points indicate the tune shift for off-momentum particles with momentum deviations of up to $\pm 1.5\%$.

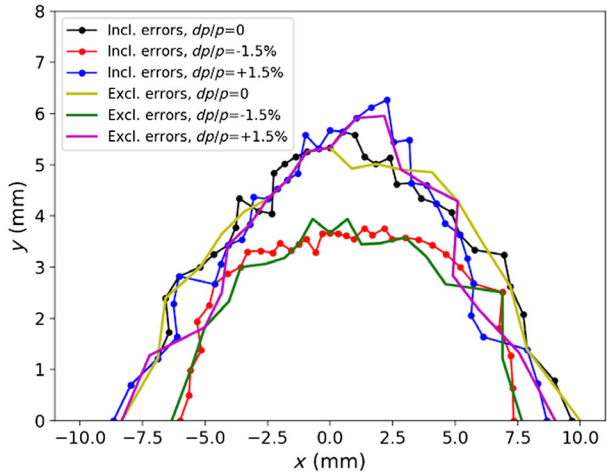

FIG. 19. Dynamic aperture of the A-PBR for perfect machine (yellow), off-momentum particles without errors (green and magenta), and including errors for different seeds (red, blue, and black). The fringe field is included in the calculations and the tracking simulations run for 26,000 turns.

fringe fields. Particles with different initial conditions were tracked, using MAD-X/PTC [41], for 26,000 turns (around 1 damping time) and the results are shown in Fig. 19, both for on-momentum ($\Delta p/p = 0$) and off-momentum ($\Delta p/p = \pm 1.5\%$) particles. Accordingly, an adequate dynamic aperture of around 7 mm in the horizontal and 4 mm in the vertical planes can be achieved.

2. Imperfections: Alignment and field errors

Magnet errors and misalignments can have a significant impact on the optics properties of the PBR, breaking the symmetry of the lattice [20,42,43]. To obtain more realistic simulations, machine misalignments (100 μm/100 μm), main field errors (10^{-3}), and systematic (summarized in Table VI) and random multipole errors (10^{-3}) were introduced for dipole, quadrupole, and sextupole magnets. The sensitivity of the A-PBR design to different sources of alignment and field errors is investigated. In this regard, the orbit and betatron-function distortions are dominated by the quadrupole alignment errors. Quadrupole misalignments and field errors are the primary sources of optics and tune distortions. In order to restore the closed orbit distortion, 188 horizontal and vertical corrector magnets were installed close to the quadrupoles, at locations with high beta functions.

The impact of imperfections on the DA was also investigated, after the closed orbit, tune, and chromaticity corrections, with results shown in Fig. 19, both for on-momentum and off-momentum particles. Comparing the results with and without errors, the dynamic aperture appears rather similar for all cases, indicating that the DA is dominated by the nonlinear effects introduced by the chromaticity sextupoles. A frequency map analysis (FMA) was also performed to identify the main resonances limiting the DA. The frequency analysis was performed using the NAFF algorithm (numerical analysis of fundamental frequencies) [44,45]. Accordingly, the fifth-order resonances seem to be the one limiting the dynamic aperture of the A-PBR. More detailed nonlinear dynamic studies would need to be performed in the future.

TABLE VI. Systematic magnet multipole errors for the A-PBR.

Element	Order	Systematic error
Dipole	2	10^{-4}
	3	1.5×10^{-4}
	4	⋯
	5	5×10^{-5}
	6	⋯
	7	5×10^{-4}
	8–20	⋯
Quadrupole	3–5	⋯
	6	10^{-6}
	7–9	⋯
	10	10^{-7}
	11–13	⋯
	14	10^{-8}
	15–17	⋯
	18	10^{-8}
	19–20	⋯
Sextupole	4–8	⋯
	9	10^{-6}
	10–14	⋯
	15	10^{-7}
	16–20	⋯

E. rf voltage and energy acceptance

As in the case of the SPS, the energy acceptance can be calculated using Eq. (5). The rf voltage program along the cycle is defined mainly by the energy loss per turn and the energy acceptance requirements. Figure 20 shows the dependence of the equilibrium energy spread σ_s (yellow), the rf voltage, V (blue), the energy loss per turn, U_0 (red), and the energy acceptance, δ_E/E (green) on the beam energy, along the PBR cycle. The energy loss per turn increases from 0.57 MeV at injection to 29.22 MeV at extraction and will, therefore, define the minimum and maximum rf voltage along the cycle. An rf voltage of 2.5 MV can provide the required 1.5% energy acceptance at injection and increases linearly up to 37 MV at extraction energy. The equilibrium rms energy spread remains at least an order of magnitude below the energy acceptance all along the cycle, which should assure an adequate quantum lifetime [38]. This condition is much more favorable than for the SPS as a prebooster.

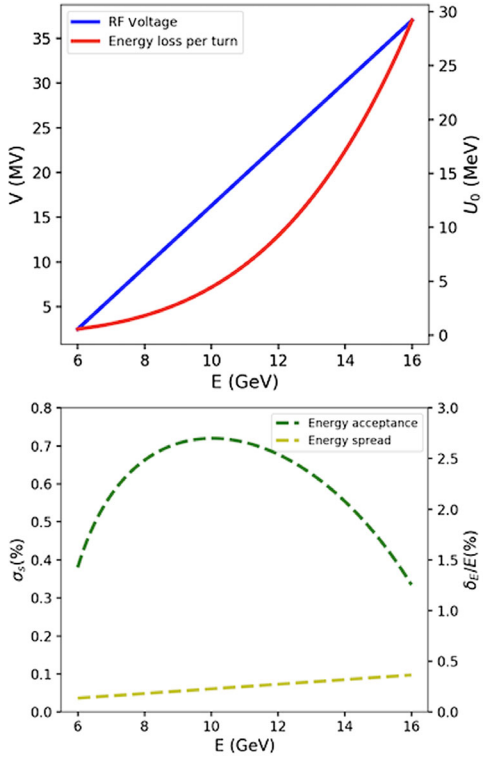

FIG. 20. Top: Energy loss per turn (U_0) (red) and rf voltage (V_{rf}) (blue) as a function of energy. Bottom: equilibrium energy spread (σ_s) (yellow) and energy acceptance ($\Delta E/E$) (green) during the energy ramping for the A-PBR.

Based on the above considerations, Table VII summarizes the main performance parameters of the A-PBR design. In this regard, a circumference of a 2-km ring with four arcs and four straight sections can achieve the requirements at injection and extraction. Adequate dynamic aperture is achieved including machine and magnet imperfections. The synchrotron radiation power studies and estimation of collective effects are also discussed in Secs. VI and VII.

VI. SYNCHROTRON RADIATION POWER CONSIDERATIONS

Synchrotron radiation (SR) power considerations should be taken into account at this early stage of the design since SR photons degrade the vacuum pressure through the process of photodesorption, and, at high energy, they may even penetrate through the vacuum chamber. The SR power can be expressed as [20]:

$$P_{\mathrm{sr}}[\mathrm{W/m}] = \frac{U_0[\mathrm{eV}]I_{\mathrm{tot}}[\mathrm{A}]}{C[\mathrm{m}]}, \tag{7}$$

where U_0 denotes the energy loss per turn, C the ring circumference, and I_{tot} the total beam current, which is proportional to the number of bunches ($I_{\mathrm{tot}} = n_b I_b$).

Table VIII summarizes the relevant parameters of the SPS-PBR and A-PBR of the FCC-ee injector complex and compares them with the case of the SPS as a LEP injector. The beam currents envisioned for the SPS-PBR are much higher than for the previous use of the SPS as a LEP injector. The effect of the damping wiggler magnets on the energy loss per turn is neglected at this point, assuming that special absorbers can be used after each wiggler magnet [46]. The maximum SR power for the SPS-PBR is considerably larger than during the LEP years [18] due to the large number of bunches and the associated high

TABLE VII. The A-PBR parameters.

Parameters	Injection		Extraction
Beam energy [E (GeV)]	6		16
Circumference [C (m)]		2030.4	
Horizontal geo. emittance [ϵ_x (nm rad)]	0.66		4.74
Damping times ($h/v/l$) [$\tau_{h/v/l}$ (s)]	0.18/0.18/0.09		0.01/0.01/0.05
Momentum spread (σ_δ)	0.3×10^{-3}		0.97×10^{-3}
Energy loss per turn [U_0 (MeV)]	0.57		29.22
Natural chromaticities (h/v) ($\xi_{h/v}$)		−99/− 59	
Bunch length [σ_z (mm)]	5.9		7.2
Tunes ($h/v/s$) ($Q_{h/v}$)		63.687/27.199	
Dynamic aperture (h/v) [DA (mm)]	6.3/3.8		⋯
rf frequency [F_{rf} (MHz)]		400	
rf voltage [V_{rf} (MV)]	2.5		37
Harmonic number (h)		2706	
Momentum compaction factor (α_c)		0.32×10^{-3}	
Energy acceptance [$\frac{\delta E}{E}$ (%)]	1.5		1.2
Bending magnet length [l_{bend} (m)]		4.1	
Field of bending [B_{dipole} (T)]	0.1		0.27
Number of bending magnets (N_{bend})		304	

TABLE VIII. Comparison of the SR parameters between the A-PBR, the SPS as LEP, and FCC-ee injector.

Parameters	SPS as LEP injector	SPS as FCC PBR	A-PBR
Extraction energy (GeV)	20	16	16
SR by dipole magnets only (excl. DW) (W/m)	1.85	198	2305
Average SR by dipole magnets only (excl. DW) (W/m)	0.024	8.1	191
SR by dipole and damping wiggler (W/m)	...	809	...
Average SR by dipole and damping wiggler (W/m)	...	107	...

beam current. The highest and average SR power of the SPS was calculated as 198 and 8.1 W/m, respectively, for the Z mode, as this is the most challenging one due to the large bunch number (see Table III). In order to accommodate such a high SR power, water-cooled gaskets or masks need to be installed in the SPS vacuum chamber. This cannot be done for the existing SPS vacuum chamber. Thus, the design and installation of a totally new vacuum system, using properly cooled chambers and absorbers, are recommended [46].

For the case of the A-PBR, the SR power is even larger due to the higher energy loss per turn and the shorter circumference. In this case, crotch absorbers after each dipole, distributed absorbers along the vacuum chamber, and special absorbers for the injection, extraction, and rf sections are required as well as a water-cooled vacuum chamber [46].

VII. COLLECTIVE EFFECT ESTIMATES

Collective effects can be a bottleneck for the performance of an accelerator, limiting its ultimate performance reach [47]. In this regard, analytical estimates related to collective effects have been performed for both the SPS-PBR and the A-PBR options including space charge (SC), longitudinal microwave instability (LMI), transverse mode coupling instability (TMCI), ion effects, electron cloud (EC), coherent synchrotron radiation (CSR), and intrabeam scattering (IBS).

A. Space charge

The incoherent tune spread caused by the space charge (SC) effect can enhance the interaction of the beam with resonances and, consequently, lead to beam degradation [44,48,49]. An analytical expression for the incoherent SC tune shift of Gaussian bunches is given by [50–52]:

$$\delta Q_y^{\mathrm{inc}} = -\frac{N_b r_e C}{(2\pi)^{\frac{3}{2}}\beta^2\gamma^3\sigma_z\sqrt{\epsilon_y}} \times \left\langle \frac{\sqrt{\beta_y}}{\sqrt{\beta_x\epsilon_x + {D_x}^2{\sigma_\delta}^2} + \sqrt{\epsilon_y\beta_y}} \right\rangle, \tag{8}$$

where r_e is the electron radius, C the circumference, N_b the bunch population, and D_x the horizontal dispersion; ϵ_x and ϵ_y denote the geometrical transverse emittances, and $\beta_{x,y}$ the horizontal and vertical betatron functions, respectively.

For flat beams, i.e., if the vertical emittance is much smaller than the horizontal one, the vertical tune spread is higher and, therefore, more critical. For the case of the PBR, the maximum value is computed at the end of the injection plateau, after the beam reaches the equilibrium emittance values in all planes. For the case of the A-PBR design, $\delta Q_y^{\mathrm{inc}} = -0.028$ while for the case of the SPS-PBR, $\delta Q_y^{\mathrm{inc}} = -0.018$. For both cases, the values are small and thus the SC is not expected to pose a limitation with respect to transverse emittance blowup or particle losses.

B. Intrabeam scattering

Intrabeam scattering (IBS) refers to multiple binary Coulomb scattering events between the particles within a beam, leading to the redistribution of the phase space. Above transition, IBS can lead to emittance blowup in all three planes [20,24,44]. Figure 21 shows the horizontal emittance evolution during the injection plateau, with (dashed lines) and without (solid lines) taking into account the IBS effect. The results for the A-PBR design are shown in red, and those for the SPS-PBR design in blue. The calculations were done using the IBS module of MAD-X [53]. The emittance growth with respect to the natural equilibrium emittance (without IBS) at the end of the injection plateau is around 6% for the A-PBR and 9% for

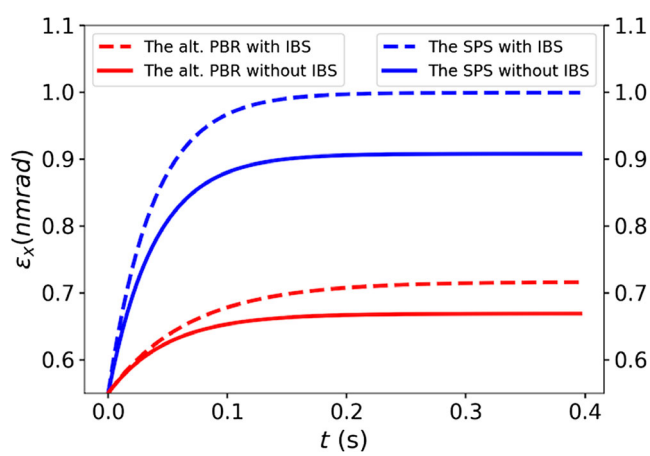

FIG. 21. Horizontal emittance evolution on the injection plateau of the SPS-PBR (blue) and the A-PBR design (red).

TABLE IX. Collective effects estimates for the SPS-PBR and the A-PBR options.

Parameters	SPS-PBR	A-PBR
SC tune shift @injection	0.0005	0.0032
SC tune shift @equilibrium	0.018	0.028
SC tune shift @extraction ($\times 10^{-4}$)	0.16	1.6
Emit. growth by IBS @injection (%)	9	6
Longitudinal impedance (Ω)	6.44	1
LMI threshold @injection (Ω)	1167	57.92
LMI threshold @equilibrium (Ω)	31.14	1.44
LMI threshold @extraction [Ω]	100	10.11
Transverse impedance (MΩ/m)	9.77	0.79
TMCI threshold @injection (MΩ/m)	29.6	5.28
TMCI threshold @equilibrium (MΩ/m)	7.10	8.95
TMCI threshold @extraction (MΩ/m)	8.97	37.0
Max. tune shift by ions	0.009	0.002
FII rise time [t_{rev}]	61	134
Chamber radius (m)	0.04	0.03
EC neutr. dens. ($10^{11}/\mathrm{m}^3$)	7.06	12.55
ECI dens. th. @injection ($10^{11}/\mathrm{m}^3$)	11.30	2.84
ECI dens. th. @equilibrium ($10^{11}/\mathrm{m}^3$)	1.62	1.43
ECI dens. th. @extraction ($10^{11}/\mathrm{m}^3$)	1.68	3.67
$0.5\rho\Lambda^{-3/2}$ (cm)	5000	0.015
ρ/b	18,525	6433
Stupakov parameter (Λ)	3.78	568

the SPS-PBR design. The effect is much smaller at extraction energy. Consequently, the IBS effect is not expected to pose a major limitation for either PBR option.

C. Longitudinal microwave instability

The geometric impedance, representing the effect of the discontinuities of the beam pipe, can cause microwave instability. According to the Boussard criterion, the corresponding (inductive) threshold impedance is given by [51,54]:

$$\frac{Z_0^{\parallel}}{n} = Z_0 \frac{\pi}{2} \frac{\gamma \alpha_c \sigma_\delta{}^2 \sigma_z}{N_b r_e} \left(\frac{b}{\sigma_z}\right)^2, \tag{9}$$

where Z_0 is the impedance of free space, and n refers to the revolution harmonic. Based on the PBR design parameters for both options, the Boussard threshold impedance $Z_0{}^{\parallel}/n$ was calculated at injection, at the end of the injection plateau, and at extraction. The results are summarized in Table IX. For the case of the A-PBR, they correspond to 57.92, 1.44, and 10.11 Ω, for the SPS-PBR design to 1167, 31.14, and 100 Ω, respectively. Historically, when used as a LEP injector, the SPS longitudinal impedance ($Z_0^{\parallel}/n$) was 6.44 Ω [55]. For the A-PBR, a 1-Ω impedance is assumed, as the design of modern accelerators can easily allow for an impedance of that magnitude or even lower. For both options, the longitudinal impedance is well below the threshold.

D. Transverse mode coupling instability

The transverse impedance of the machine can drive the head-tail instability (HTI) and/or the transverse mode coupling instability (TMCI) [51]. The TMCI threshold for a broadband resonator impedance is given by [51,54]:

$$R_{\mathrm{th}}[\mathrm{k}\Omega/\mathrm{m}] = \frac{0.6E[\mathrm{GeV}]Q_s Q}{\beta_y[\mathrm{m}]Q_b[\mathrm{C}]\sigma_t[\mathrm{ps}]f_r^2[\mathrm{GHz}]}, \tag{10}$$

where $Q_b = N_b e$, $f_r = W_r/(2\pi)$, $W_r = c/b$, $\sigma_t = \sigma_z/c$. The thresholds for both designs were estimated at injection, at the end of the injection plateau, and at extraction and correspond to 5.3, 8.9, and 37.0 MΩ/m for the A-PBR and to 29.6, 7.1, and 9 MΩ/m for the SPS-PBR. The transverse impedance can be roughly linked to the longitudinal impedance through [44,50]:

$$Z_t{}^{\perp} = \frac{C}{\pi b^2} \frac{Z_0{}^{\parallel}}{n}. \tag{11}$$

Based on this, the transverse impedance ($Z_t{}^{\perp}$) of the A-PBR is estimated as 0.8 MΩ/m, which is well below the calculated threshold. On the other hand, the transverse impedance for the case of the SPS-PBR is estimated at 9.8 MΩ/m, which is above the threshold computed at the end of the injection plateau and at extraction. The necessary new elements for the e^+/e^- option of the SPS-PBR (rf, transfer elements, vacuum, etc.) need to be designed taking into account these impedance considerations. At the same time, they must also allow for seamless proton beam operation.

E. Ion effects

Ions can be created in the vacuum chamber through the interaction of charged beam particles with the residual gas in the beam pipe. These ions can be trapped and accumulated by the fields of the electron beam. Eventually, they can result in beam instability [56–58]. The critical mass for the trapping of a singly charged ion is [50,51]:

$$A_{\mathrm{crit}} \cong \frac{N_b \Delta T_b c r_p}{2\sigma_y(\sigma_x + \sigma_y)}, \tag{12}$$

where r_p is the classical proton radius and ΔT_b the bunch spacing. Ions with a mass A higher than the critical mass will be trapped in the field of the beam.

Figure 22 shows the critical mass computed for the A-PBR (top) and the SPS-PBR (bottom) as well as the thresholds for different ions. The critical mass is lower than the mass of almost all possible types of ions generated inside the vacuum chamber, for both PBR options. Ions

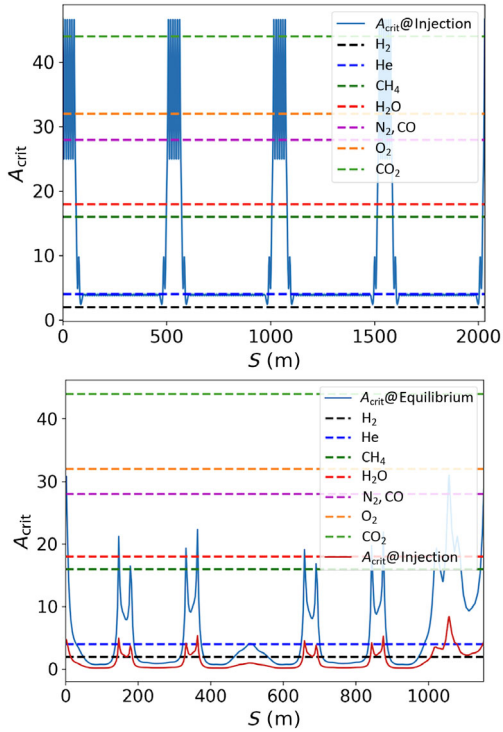

FIG. 22. Critical mass for the A-PBR (top) and one sextant of the SPS-PBR (bottom) in comparison to the thresholds for various molecules.

trapped by the electron beam induce a tune shift, which at the end of a bunch train becomes [50,51,56]:

$$\delta Q_{\rm ion} \cong \frac{N_b n_b r_e C}{\pi\gamma\sqrt{\epsilon_x\epsilon_y}}\left(\frac{\sigma_{\rm ion} p}{k_B T}\right), \tag{13}$$

where $\sigma_{\rm ion}$ is the ionization cross section, p is the vacuum pressure, and k_B is the Boltzmann constant. For the A-PBR $\delta Q_{\rm ion} = 0.002$ while for the SPS-PBR $\delta Q_{\rm ion} = 0.009$, which are both relatively small, assuming a pressure of 10^{-10} mbar for the A-PBR and 10^{-11} mbar for the SPS-PBR, which may drive pumping upgrade considerations.

The accumulated ions can lead to fast-ion instability (FII) with a rise time given by [50,51,56,57]:

$$\tau_{\rm inst} \cong \frac{0.1\gamma\sigma_x\sigma_y}{N_b n_b c r_e \beta_y \sigma_{\rm ion}}\left(\frac{k_B T}{p}\right)\left(\sqrt{\frac{8}{\pi}}\right). \tag{14}$$

The FII rise times are obtained as 61 and 134 revolution times ($t_{\rm rev}$) for the SPS-PBR and the A-PBR, respectively. Instabilities with such rise times can be suppressed by a feedback system, provided that vacuum pressures of 10^{-11} mbar for the SPS-PBR and 10^{-10} mbar for the A-PBR are achieved.

F. Electron cloud

The electron cloud instability (ECI) mostly arises for e^+ beams [57,59]. When free electrons in the vacuum chamber get accelerated in the electromagnetic field of the beam and hit the chamber walls, electron amplification can occur through the multipacting effect. The e^- buildup saturates when the attractive beam field is compensated by the field of the electrons, at a neutralization density, given by [57]:

$$\rho_{\rm neutr} = \frac{N_b}{L_{\rm sep}\pi b_x b_y}, \tag{15}$$

where $L_{\rm sep}$ [m] is the bunch spacing. Electron cloud can lead to single or coupled-bunch instabilities. The single bunch ECI occurs above the e^- density threshold estimated by [57,60,61]:

$$\rho_{\rm th} = \frac{2\gamma Q_s}{\sqrt{3} Q r_e \beta_y C}, \tag{16}$$

where $Q = \min(7, \omega_e\sigma_z/c)$ is the angular oscillation frequency of the electrons interacting with the beam, with ${\omega_e}^2 = N_b r_e c^2/[2\sigma_z\sigma_y(\sigma_x+\sigma_y)]$. The neutralization densities for both the A-PBR and the SPS-PBR options were calculated as $12.55\times10^{11}/{\rm m}^3$ and $7.06\times10^{11}/{\rm m}^3$, respectively. The neutralization density exceeds the instability threshold for both designs (see Table IX). This aspect, and in particular possible mitigation measures, should be investigated with detailed simulations in the following phases of the FCC project.

G. Coherent synchrotron radiation

Coherent synchrotron radiation (CSR) occurs if the SR wavelength is comparable to the bunch length. The CSR may lead to a microbunching instability under the following conditions [44,62–65]:

$$\sigma_z \geq 0.5\rho\Lambda^{-3/2} \quad \text{and} \quad \rho/b \leq \Lambda, \tag{17}$$

where b is the chamber radius, ρ the bending radius, and Λ known as the Stupakov-Heifets parameter:

$$\Lambda = \frac{N_b r_e \rho\sqrt{2\pi}}{C|\alpha_c|\sigma_z\gamma{\sigma_\delta}^2}. \tag{18}$$

The instability conditions were calculated for both design options and presented in Table IX, indicating that no CSR instability is expected.

H. Summary of collective effect study

In this section, analytical estimates of various collective effects were presented for the two FCC-ee PBR design options. Based on these estimates, no major limitations are expected due to SC, IBS, LMI and CSR. Concerning the TMCI, the transverse impedance exceeds the instability threshold for the SPS-PBR. Furthermore, it was shown that the neutralization density exceeds the ECI threshold

for both design options. The fast rise times computed for the FII can be compensated by a feedback system, provided that a vacuum pressure of 10^{-11} and 10^{-10} mbar can be achieved for the SPS-PBR and the A-PBR design, respectively.

VIII. CONCLUSION

Two FCC-ee prebooster ring design options have been developed. One is based on the existing SPS with a few necessary modifications (SPS-PBR) and the alternative is a green-field ring design (A-PBR).

For the SPS-PBR option, two main challenges were addressed. Namely, the horizontal equilibrium emittance at extraction and the damping time at injection are both considerably larger than the required values. In this regard, a phase advance optimization was performed and the insertion of a combination of damping and Robinson wiggler magnets was proposed. After these modifications, both the required emittance at extraction and damping time at injection could be demonstrated. As a side effect of the optimization, the equilibrium rms energy spread at extraction is quite high compared with the longitudinal acceptance. Consequently, a much higher rf voltage than hitherto assumed may turn out to be necessary. Dynamic aperture simulations were also carried out, including sextupoles and fringe fields, demonstrating an adequate dynamic aperture in both planes. In addition, the rf voltage program along the cycle was defined for achieving the required energy acceptance, including a good injection efficiency. Analytical estimations for various collective effects were also made, and the main limitations were identified. The SPS transverse impedance exceeds the calculated instability threshold, which needs to be taken into account when modifying the SPS beam vacuum chambers and in the design of new elements for the e^+/e^- option. The fast ion instability can be compensated with a feedback system, provided that the current vacuum pressure of the SPS is considerably improved; furthermore, it was shown that the neutralization density exceeds the electron cloud instability threshold. For this point, more detailed simulations should follow. Synchrotron radiation power calculations demonstrate that the design of a totally new vacuum system is required as the existing one cannot sustain the expected synchrotron radiation power. In summary, although the existing SPS ring has limitations such as availability and minimum modification possibility, the required parameters could be provided by using insertion devices. It is convenient to have an already working machine in terms of cost-based evaluation; however, it could also be taken into account that the vacuum system should be replaced (with properly cooled chambers and absorbers) and a superconducting damping wiggler is needed to reach the required parameters. Furthermore, a challenging rf system is needed.

For the A-PBR option, the conceptual design of an alternative prebooster ring option was presented. A ring layout was defined based on a parameter scaling: a ring circumference of around 2 km with four arcs and four straight sections was finally chosen. The linear optics design was presented. Based on this design, the required beam characteristics at extraction from the PBR can be achieved. First nonlinear dynamics considerations were also discussed. An adequate DA was demonstrated, dominated by the nonlinear effects introduced by the sextupoles used for the chromatic correction. The impact of alignment errors and magnet imperfections on the dynamic aperture of the machine was also investigated and the effect was proven to be small. In addition, collective effects were estimated and the main limitations were identified: As for the SPS-PBR, the neutralization density exceeds the calculated electron cloud instability threshold and, again, more detailed simulations should be performed in the future; an ultralow vacuum pressure is required in order to avoid uncontrolled fast ion instabilities. Finally, synchrotron radiation power calculations were executed: during the design process, special attention should be paid to the vacuum chambers of this new machine. The A-PBR design may require a much lower rf voltage than the SPS option, for achieving a decent quantum lifetime. In summary, the required parameters could be achieved with a comparatively short ring without using any insertion devices. A-PBR does not have the existing machine limitations; however, the cost of building such a machine is incontrovertible.

Both prebooster ring options, SPS-PBR and A-PBR design, have eventually met the required parameters of the FCC-ee injector complex, each with its own advantages and disadvantages. In terms of the scientific perspective, both designs are compatible with the project demands. One of them could be chosen as the baseline for the next phase of the FCC project.

ACKNOWLEDGMENTS

We would like to thank Ji Li for his help and his experience with Robinson wiggler magnets, Masamitsu Aiba for useful discussions on the injection methods, Roberto Kersevan for his warm help on synchrotron radiation calculations and vacuum chamber constraints, Hannes Bartosik for his help with the latest SPS design and nonlinear chromaticity, the participants of the regular FCC-ee injector and FCC-ee optics meetings members for many useful discussions and feedback during the design process. We acknowledge support from the FCC design study hosted at CERN and the global FCC Collaboration.

[1] A. Abada, M. Abbrescia, S. S. AbdusSalam, I. Abdyukhanov, J. Abelleira Fernandez, A. Abramov, M. Aburaia, A. O. Acar, P. R. Adzic, P. Agrawal *et al.*,

$FCC-e^+e^-$: The Lepton Collider, Eur. Phys. J. Spec. Top. **228**, 261 (2019).

[2] A. Abada, M. Abbrescia, S. S. AbdusSalam, I. Abdyukhanov, J. Abelleira Fernandez, A. Abramov, M. Aburaia, A. O. Acar, P. R. Adzic, P. Agrawal *et al.*, $FCC-hh$: The Hadron Collider, Eur. Phys. J. Spec. Top. **228**, 755 (2019).

[3] A. Abada, M. Abbrescia, S. S. AbdusSalam, I. Abdyukhanov, J. Abelleira Fernandez, A. Abramov, M. Aburaia, A. O. Acar, P. R. Adzic, P. Agrawal *et al.*, HE-LHC: The High-Energy Large Hadron Collider, Eur. Phys. J. Spec. Top. **228**, 1109 (2019).

[4] A. Abada, M. Abbrescia, S. S. AbdusSalam, I. Abdyukhanov, J. Abelleira Fernandez, A. Abramov, M. Aburaia, A. O. Acar, P. R. Adzic, P. Agrawal *et al.*, FCC physics opportunities, Eur. Phys. J. C **79**, 474 (2019).

[5] K. Oide, M. Aiba, S. Aumon, M. Benedikt, A. Blondel, A. Bogomyagkov, M. Boscolo, H. Burkhardt, Y. Cai, A. Doblhammer *et al.*, Design of beam optics for the future circular collider e^+e^- collider rings, Phys. Rev. Accel. Beams **19**, 111005 (2016).

[6] S. Ogur, F. Antoniou, T. K. Charles, O. Etisken, B. Harer, B. Holzer, K. Oide, T. Tydecks, Y. Papaphilippou, L. Rinolfi *et al.*, Overall injection strategy for $FCC-e^+e^-$, in *Proceedings of 62nd ICFA ABDW on High Luminosity Circular e^+e^- Colliders, eeFACT2018, Hong Kong, China* (JACoW, Geneva, Switzerland, 2018), TUPAB03.

[7] K. Cornelis and R. Schmidt, The performance of the SPS as LEP injector, in *Proceedings of the 1989 Particle Accelerator Conference, Chicago, IL* (IEEE, New York, 1989).

[8] M. Benedikt, V. M. P. Collier, J. Poole, K. Schindl *et al.*, LHC design report, Vol. III: The injector chain (CERN, 2004).

[9] V. Kain, H. Bartosik, S. Cettour-Cave, K. Cornelis, M. A. Fraser, L. Gatignon, B. Goddard, and F. Velotti, Fixed target beams, in *Injector MD Days 2017*, Vol. 2 (CERN Proceedings, Switzerland, 2017).

[10] O. Etisken, Y. Papaphilippou, F. Antoniou, T. Tydecks, and A. K. Ciftci, Updates on alternative pre-booster ring design and Wiggler magnet considerations of SPS for the FCC-e^+e^- injector, in *Proceedings of 10th International Particle Accelerator Conference, IPAC19, Melbourne, Australia* (JACoW, Geneva, Switzerland, 2019).

[11] S. Ogur, T. Charles, K. Oide, Y. Papaphilippou, L. Rinolfi, F. Zimmermann, A. Barnyakov, A. Levichev, P. Martyshkin, D. Nikiforov *et al.*, Layout and performance of the $FCC-e^+e^-$ pre-injector chain, in *Proceedings of 9th International Particle Accelerator Conference, IPAC'18, Vancouver, BC, Canada* (JACoW, Geneva, Switzerland, 2018), pp. 169–172.

[12] S. Ogur, Linac and damping ring designs of the Future Circular e^+e^- Collider of CERN, Ph.D. thesis, Bogazici University, 2019.

[13] O. Etisken, N. Mounet, A. Oeftiger, S. Ogur, K. Oide, Y. Papaphilippou, B. Salvant, and F. Zimmermann, Damping bunch oscillation due to off-axis injection, in *Proceedings of 10th International Particle Accelerator Conference, IPAC-2019, Melbourne, Australia* (JACoW, Geneva, Switzerland, 2019).

[14] Masamitsu Aiba, Geneva, Switzerland (personal communication).

[15] Y. Papaphilippou, F. Zimmermann, K. Oide, L. Rinolfi, and D. Shwartz, Design guidelines for the injector complex of the FCC-e^+e^- injector, in *Proceedings of 7th International Particle Accelerator Conference, IPAC-2016, Busan, Korea* (JACoW, Geneva, Switzerland, 2016), THPMR042.

[16] B. Haerer, B. Holzer, and Y. Papaphilippou, Status of the FCC-e^+e^- top-up booster synchrotron, in *Proceedings of 9th International Particle Accelerator Conference, IPAC-2018, Vancouver, Canada* (JACoW, Geneva, Switzerland, 2018).

[17] J. Gareyte, Performance of the CERN SPS as a Proton-Antiproton Collider, in *Proceedings of 12th International Conference on High-Energy Accelerators* (CERN-SPS-83-28-DI-MST, 1983).

[18] LEP design report, CERN, Report No. CERN-LEP-TH-83-29, The LEP injector chain (by the LEP Injector Study Group, 1983).

[19] Y. Papaphilippou, R. Corsini, and L. Evans, The SPS as an ultra-low emittance Damping Ring Test Facility for CLIC, in *Proceedings of 4th International Particle Accelerator Conference, IPAC-2013, Shanghai, China, 2013* (JACoW, Shanghai, China, 2013).

[20] H. Wiedemann, *Particle Accelerator Physics* (Springer, New York, 2015).

[21] S. Y. Lee, *Accelerator Physics* (World Scientific, Singapore, 2015).

[22] O. Etisken, F. Antoniou, A. K. Ciftci, and Y. Papaphilippou, Prebooster ring considerations for FCC e^+e^- injector, in *Proceedings of 9th International Particle Accelerator Conference, IPAC18, Vancouver, BC, Canada* (JACoW, Geneva, Switzerland, 2018).

[23] A. Wolski, The accelerator physics of linear collider damping rings, in *Notes for USPAS Course on Linear Colliders* (USPAS Course Materials, Santa Barbara, 2003).

[24] F. Antoniou, Optics design of intra-beam scattering dominated damping rings, Ph.D. thesis, National Technical University of Athens, 2012.

[25] K. W. Robinson, Radiation effects in circular electron accelerators, Phys. Rev. **111**, 373 (1958).

[26] T. Tydecks, A Robinson wiggler for the Metrology Light Source, Ph.D. thesis, Humboldt-Universität zu Berlin, 2016.

[27] H. Abualrob, P. Brunelle, M. E. Couprie, M. Labat, A. Nadji, N. S. Nadolski, and O. Marcouille, Horizontal emittance reduction on a synchrotron radiation light source with a Robinson wiggler, arXiv:1806.09354.

[28] T. Goetsch, J. Feikes, M. Ries, and G. Wustefeld, A Robinson wiggler proposal for the Metrology Light Source, in *Proceedings of 5th International Particle Accelerator Conference, IPAC-2014, Dresden, Germany* (JACoW, Geneva, Switzerland, 2014), WEPRO028.

[29] Y. Baconnier, R. Cappi, J. Riunaud, and H. Umstatter, Emittance control of the PS e^+e^- beams using a Robinson wiggler, Nucl. Instrum. Methods Phys. Res., Sect. A **234**, 244 (1985).

[30] T. Goetsch, J. Feikes, M. Ries, and G. Wustefeld, Status of the Robinson wiggler project at the Metrology Light

Source, in *Proceedings of 6th International Particle Accelerator Conference, IPAC-2015, Richmond, VA* (JACoW, Geneva, Switzerland, 2015), MOPWA019.

[31] H. Abualrob, P. Brunelle, M.-E. Couprie, O. Marcouille, A. Nadji, L. Nadolski, and R. Nagaoka, SOLEIL emittance reduction using a Robinson Wiggler, in *Proceedings of 3rd International Particle Accelerator Conference IPAC-2012, New Orleans* (JACoW, Geneva, Switzerland, 2012), MOPPP062.

[32] M. Aiba, Review of top-up injection schemes for Electron Storage Rings, in *Proceedings of 9th International Particle Accelerator Conference IPAC-2018, Vancouver, BC, Canada* (JACoW, Geneva, Switzerland, 2018), WEXGBE1.

[33] M. Aiba, Top-up injection scheme, in *FCC Week 2017* (FCC Week Presentations, Berlin, Germany, 2017).

[34] A. Wolski, A new lattice design for the NLC positron pre-damping ring, in *Proceedings of the 8th European Particle Accelerator Conference, Paris, 2002* (EPS-IGA and CERN, Geneva, 2002).

[35] K. Wille, *The Physics of Particle Accelerators: An Introduction* (Oxford University Press, Oxford, New York, 2005).

[36] P. J. Bryant and K. Johnsen, *The Principles of Circular Accelerators and Storage Rings* (Cambridge University Press, Cambridge, England, 2005).

[37] V. Kain, R. Alemany-Fernandez, H. Bartosik, S. C. Cave, K. Cornelis, P. Cruikshank, J. F. Somoza, B. Goddard, and C. Pasquino, Identification and removal of SPS aperture limitations, in *Proceedings of 9th International Particle Accelerator Conference, IPAC-2018, Vancouver, BC, Canada* (JACoW, Geneva, Switzerland, 2018), TUPAF021.

[38] M. Sands, The physics of electron storage rings: An introduction, SLAC-121 (1971), https://cds.cern.ch/record/102780.

[39] B. Haerer, S. Aumon, B. Holzer, K. Oide, Y. Papaphilippou, and T. Tydecks, Challenges and status of the rapid cycling top-up booster for FCC-ee, in *Proceedings of 8th International Particle Accelerator Conference (IPAC'17)* (Jacow Publishing, Denmark, 2017).

[40] E. Forest and J. Milutinovic, Leading Order Hard Edge Fringe Fields Effects Exact in $(1+\delta)$ and Consistent with Maxwells Equations for Rectilinear Magnets, Nucl. Instrum. Methods Phys. Res., Sect. A **269**, 474 (1998).

[41] CERN, MAD-X/PTC (The Polymorphic Tracking Code), CERN-BE/ABP Accelerator Beam Physics Group, 2020.

[42] H. Ghasem, F. Antoniou, J. Alabau-Gonzalvo, S. Papadopoulou, and Y. Papaphilippou, Nonlinear optimization of CLIC DRs new design with variable bends and high field wigglers, in *Proceedings of 7th International Particle Accelerator Conference, IPAC-2016, Busan, Korea* (JACoW, Geneva, Switzerland, 2016), WEPMW003.

[43] Y. Renier, F. Antoniou, H. Bartosik, Y. Papaphilippou, and K. Wootton, Non-linear dynamics optimization of the CLIC damping rings, in *Proceedings of 2nd International Particle Accelerator Conference, IPAC-2011, San Sebastian, Spain* (JACoW, Geneva, Switzerland, 2011).

[44] A. Wolski, *Beam Dynamics in High Energy Particle Accelerators* (Imperial College Press, London, 2014).

[45] J. Laskar, Frequency map analysis and particle accelerators, in *Proceedings of the 20th Particle Accelerator Conference, PAC-2003, Portland, OR, 2003* (IEEE, New York, 2003).

[46] Roberto Kersevan, Geneva, Switzerland (personal communication).

[47] A. W. Chao, *Physics of Collective Beam Instabilities in High Energy Accelerators* (Wiley Interscience, New York, 1993).

[48] M. Ferrario, M. Migliorati, and L. Palumbo, Space charge effects, in *Proceedings of the CAS-CERN Accelerator School: Advanced Accelerator Physics*, CERN-2014-009 (CAS, Norway, 2013).

[49] W. T. Weng, Space charge effects-tune shifts and resonances, CAS, Report No. SLAC-PUB–4058, 1986.

[50] F. Zimmermann, M. Korostelev, D. Schulte, T. Agoh, and K. Yokoya, Collective effects in the CLIC damping rings, in *Proceedings of the 11th European Particle Accelerator Conference, Genoa, 2008* (EPS-AG, Genoa, Italy, 2008), MOPP049.

[51] G. Rumolo, J. Jeanneret, Y. Papaphilippou, and D. Quatraro, Collective effects in the CLIC damping rings, in *Proceedings of the 11th European Particle Accelerator Conference, Genoa, 2008* (EPS-AG, Genoa, Italy, 2008).

[52] K. Schindl, Space charge, in *Proceedings of CAS—CERN Accelerator School: Basic Course on General Accelerator Physics* (CAS, Montreux, Switzerland, 1998).

[53] CERN, MAD-X (Methodical Accelerator Design), CERN-BE/ABP Accelerator Beam Physics Group, 2020.

[54] E. Koukovini-Platia, K. Li, N. Mounet, G. Rumolo, and B. Salvant, Impedance effects in the CLIC damping rings, in *Proceedings of 2nd International Particle Accelerator Conference, IPAC-2011, San Sebastian, Spain* (JACoW, Geneva, Switzerland, 2011).

[55] D. Brandt, E. Brouzet, K. Cornelis, J. Gareyte, W. Herr, R. J. Lauckner, T. P. Linnecar, and R. Schmidt, Beam dynamics effects in the CERN SPS used as a Lepton Accelerator, in *Proceedings of 13th Particle Accelerator Conference, PAC89* (IEEE, New York, 1989), CERN-SPS-89/6.

[56] F. Zimmermann, J. Byrd, A. Chao, S. Heifets, M. Minty, T. Raubenheimer, J. Seeman, G. Stupakov, and J. Thomson, Experiments on the fast beam-ion instability at the ALS, in *Proceedings of International Workshop on Multibunch Instabilities in Future Electron and Positron Accelerators, MBI97* (Report No. SLAC-PUB-7617, 1997).

[57] F. Zimmermann, Two-stream effects in present and future accelerators, in *Proceedings of the 8th European Particle Accelerator Conference, Paris, 2002* (EPS-IGA and CERN, Geneva, 2002).

[58] R. Nagaoka, Ions, in *Proceedings of the CAS-CERN Accelerator School: Intensity Limitations in Particle Beams* (CERN Yellow Reports, Switzerland, 2017), Vol. 3.

[59] G. Rumolo and G. Iadarola, Electron clouds, in *Proceedings of the CAS-CERN Accelerator School: Intensity Limitations in Particle Beams* (CERN Yellow Reports, Switzerland, 2017), Vol. 3.

[60] E. Belli, P. C. Pinto, G. Rumolo, T. Sinkovits, M. Taborelli, and M. Migliorati, Electron cloud studies in FCC-e^+e^-, in

Proceedings of 9th International Particle Accelerator Conference, IPAC2018, Vancouver, BC, Canada (JACoW, Geneva, Switzerland, 2018), MOPMK012.

[61] K. Ohmi and F. Zimmermann, Study of coherent tune shift caused by electron in positron storage rings, in *Proceedings of the Second Asian Particle Accelerator Conference, Beijing, China* (SLAC-PUB-9079, CERN-SL-2001-062-AP, 2001).

[62] G. Stupakov and S. Heifets, Beam instability and microbunching due to coherent synchrotron radiation, Phys. Rev. ST Accel. Beams **5**, 054402 (2002).

[63] G. Stupakov and S. Heifets, Beam instability and microbunching due to coherent synchrotron radiation, SLAC National Accelerator Laboratory, Report No. SLAC-PUB-8761, 2001.

[64] C.-Y. Tsaiy, Suppressing CSR microbunching in recirculation arcs, in *Proceedings of 9th International Particle Accelerator Conference, IPAC-2018, Vancouver, BC, Canada* (JACoW, Geneva, Switzerland, 2001).

[65] F. Zimmermann, Estimates of CSR instability thresholds for various storage rings, CERN, Report No. ATS-Note-2010-049, CLIC-Note-861, 2001.